Assessing the carbon sequestration potential of basalt using X-ray micro-CT and rock mechanics

by

Ben Callow[1*]

Ismael Falcon-Suarez [2]

Sharif Ahmed[3]

&

Juerg Matter[1]

(1) University of Southampton, Ocean and Earth Science, Southampton, SO14 3ZH, UK.

(2) National Oceanography Centre, University of Southampton Waterfront Campus, European Way, Southampton, SO14 3ZH, UK.

(3) µ-VIS X-Ray Imaging Centre, Faculty of Engineering and the Environment, University of Southampton, University Road, Southampton, SO17 1BJ, UK.

Accepted article:

"International Journal of Greenhouse Gas Control"

Volume 70, March 2018, Pages 146-156

DOI: https://doi.org/10.1016/j.ijggc.2017.12.008

*Corresponding author: University of Southampton, Ocean and Earth Science, Southampton, SO14 3ZH, UK.

Phone: +44 (0)7772657517 Office: 184/13 email: Ben.Callow@noc.soton.ac.uk

Abstract

Mineral carbonation in basaltic rock provides a permanent storage solution for the mitigation of anthropogenic CO_2 emissions in the atmosphere. 3D X-ray micro-CT (XCT) image analysis is applied to a core sample from the main basaltic reservoir of the CarbFix site in Iceland, which obtained a connected porosity of 2.05–8.76 %, a reactive surface area of 0.10-0.33 mm^{-1} and a larger vertical permeability (2.07×10^{-10} m^2) compared to horizontal permeability (5.10×10^{-11} m^2). The calculations suggest a CO_2 storage capacity of 0.33 Gigatonnes at the CarbFix pilot site. The XCT results were compared to those obtained from a hydromechanical test applied to the same sample, during which permeability, electrical resistivity and volumetric deformation were measured under realistic reservoir pressure conditions. It was found that permeability is highly stress sensitive, dropping by two orders of magnitude for a -0.02% volumetric deformation change, equivalent to a mean pore diameter reduction of 5 µm. This pore contraction was insufficient to explain such a permeability reduction according to the XCT analysis, unless combined with the effects of clay swelling and secondary mineral pore clogging. The findings provide important benchmark data for the future upscaling and optimisation of CO_2 storage in basalt formations.

Key words: *CO_2 sequestration, Geological storage, basalt, permeability, X-Ray micro-CT, image-based modelling*.

1. Introduction

Mineralisation of CO_2 in basaltic rock formations may provide an effective method of CO_2 sequestration (CCS) (Oelkers et al., 2008, Gislason et al., 2010, Matter et al., 2016), mitigating increased anthropogenic CO_2 emissions in the atmosphere. Basalt has enormous CO_2 storage potential, comprising ~60 % of the Earth's surface, and storage capactities of ~13,800 to 127,800 Gt of CO_2 have been estimated in deep-sea basalt reservoirs (Gislason et al., 2010; Marieni et al., 2013). CCS in basalt encourages mineral trapping, also referred to as in situ carbonation, providing a permanent storage solution (Sigfusson et al., 2015). Compared to CCS in basalts, conventional CCS in sedimentary rock (e.g. sandstones) requires extensive monitoring and high cap rock integrity, which can degrade over time due to CO_2-fluid-rock interactions (Gaus, 2010).

The CarbFix project at the Hellisheidi geothermal power plant in Iceland is an onshore example of a pilot study in which the mineral carbonation of CO_2 potential of basaltic rocks is investigated (Figure 1). 40,000 tons of CO_2 per year is currently produced by Hellisheidi geothermal power plant (Sigfusson et al., 2015). In addition, Iceland is composed of ~90 % basaltic rocks, providing the ideal location for the pilot study (Hjartarson and Sæmundsson, 2014; Snæbjörnsdóttir et al., 2014). The target formation is composed of basalt lavas with an olivine tholeiite composition, ranging in age from 500,000 to 125,000 years before present, with a low degree of secondary alteration (Alfredsson et al., 2013).

In January 2012, 230 tons of CO_2 was coinjected with 7000 tons of H_2O into injection well HN-02 (Matter et al., 2016). To allow distinction between native carbon in the basalt reservoir and injected CO_2, Carbon-14 (^{14}C) in the form $NaH^{14}CO^{-}_3$, in addition to non-reactive SF6 and SF5CF3 tracers, were coinjected with the injected

CO_2 (Matter et al., 2013). Proximal to the injection site, the injected CO_2 and H_2O react to form carbonic acid. The dissolution of secondary mineral phases, primary host rock minerals and basaltic glass occurs due to the flow of low pH injection waters. Secondary carbonates are expected to precipitate further from the injection site as reactions (1-2) proceed to the right (Alfredsson et al., 2013):

$$CO_2 + H_2O = H_2CO_3 \tag{1}$$

$$(Fe, Ca, Mg)^{2+} + H_2CO_3 = (Fe, Ca, Mg)CO_3 + 2H^+ \tag{2}$$

To characterise storage reservoir parameters subsequent to the injection, 150 m of core KB-01 have been drilled between injection well HN-02 and monitoring well HN-04 (Figure 1). From geochemical studies using the tracers, >95 % of the injected CO_2 is believed to have mineralised between wells HN-02 and HN-04, within a couple of months of the initial CO_2 injection (Matter et al., 2016).

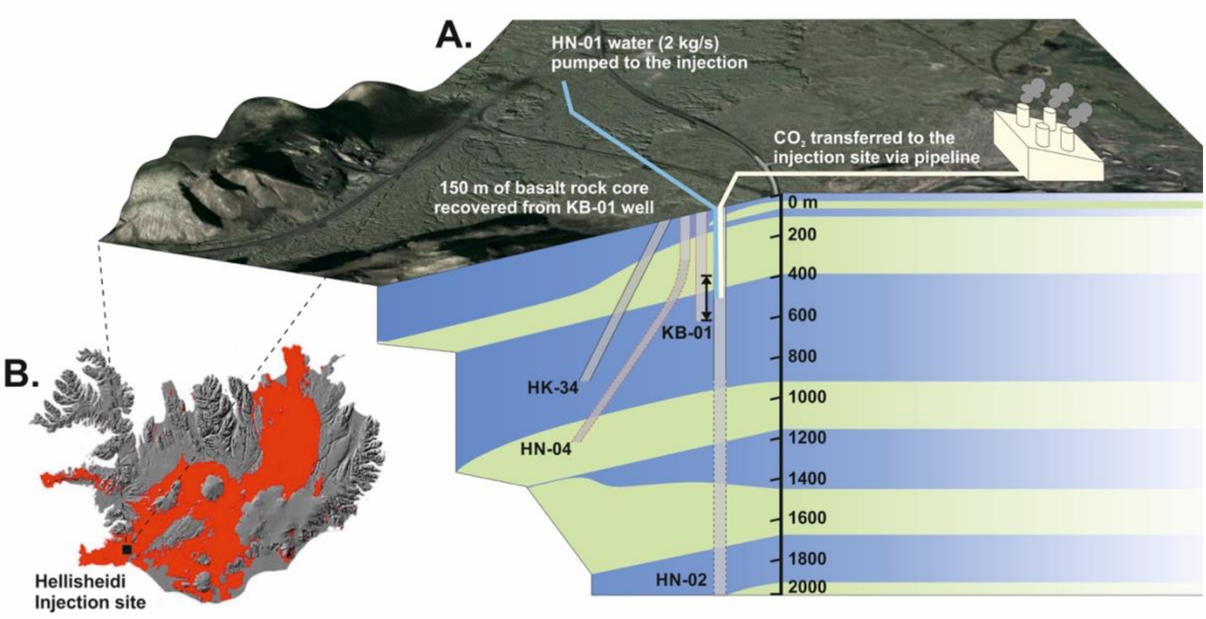

Figure 1. A. A geological cross section of the Hellisheidi injection site, showing the location of drill core KB-01. Blue represents basalt rock and green represents hyaloclastite formations. 150 m of core

section have been taken from the basalt CO_2 storage formation. The drill core is located between injection well HN-02 and monitoring well HN-04, which are 10 m apart at the surface. The figure is modified from Alfredsson et al. (2013). **B**. The location of Hellisheidi injection site is shown on a map of Iceland. The area in red highlights basaltic rock formations < 0.8 Myr within the active rift zone. These basalt rock formations are expected to have the greatest reservoir potential due to a low degree of secondary mineralisation and compaction. The figure is modified from Snæbjörnsdóttir et al. (2014).

Up to now there has been a lack of research undertaken to characterise the reservoir properties of basalt. In previous reservoir scale studies by Khalilabad et al. (2008) using a Na-Fluorescein tracer it was found that only 3% of the injected tracer was channelled by a discrete fracture system between HN-02 and HN-04. The remaining injected tracer was interpreted to have flowed through the vesicles (matrix flow), highlighting the importance of understanding matrix flow in the basalt reservoir (Gislason et al. 2010). In this study we characterise the reservoir properties of the target basalt formation at Hellisheidi through the analysis of porosity, reactive surface area, pore network modelling and the permeability of KB-01 core samples using X-Ray micro-CT (computer tomography) and hydromechanic flow-through tests on a laboratory scale. The ultimate aim is to provide a reliable and robust quantification of the CO_2 sequestration potential of the basalt rock reservoir. This is the first ever study to combine analysis of a vesicular pore network of basalt rock using 3D X-ray micro-computed tomography, connected (effective) porosity determinations and reactive surface area values for calculations of CO_2 mineral carbonation. The ultimate aim of this work is to provide a reliable and robust quantification of the CO_2 sequestration potential of basalt rock reservoirs. The study also highlights a number of important issues regarding the potential effect of secondary mineral pore clogging in the presence of high salinity fluids, of great importance since the most suitable basaltic CO_2 storage sites are found offshore (Goldberg and Slagle, 2009).

2. Materials and Methods

2.1. X-Ray Micro-CT analysis

2.1.1. Image acquisition

3D X-ray micro-CT (XCT) scans were conducted using a micro-focus Custom Nikon HMX ST Scanner at the µ-VIS X-Ray Imaging Centre, University of Southampton. The scanner has a 225 kV X-ray source and a 2000 x 2000 pixel flat panel dector (Figure 2).

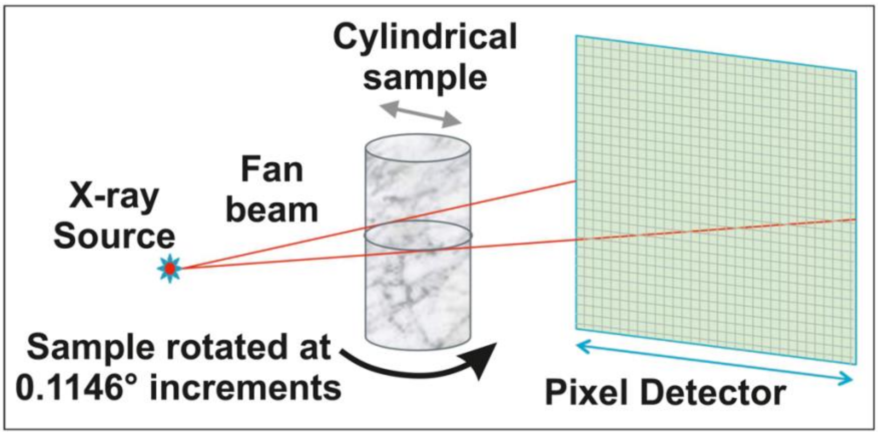

Figure 2. Diagram of the micro-computer tomography (micro-CT) imaging of the core samples. X-rays propagate through the sample with a fan geometry from the X-ray source and are detected by a 2 x 2000 pixel detector. 2D image slices are reconstructed from projections made at 0.1146º increments, to produce a 3D volume.

Data was acquired using an electron accelerating potential of 200 kV and a tube current of 128 µA. The X-ray beam was filtered using 0.250 mm of tin. 3143 equiangular projections were acquired through 360° with 8 frames per projection taken to reduce noise. 3D reconstruction of the projections was performed using a proprietary filtered back-projection algorithm implemented in CTPro 3D (Nikon Metrology, Tring, UK). The reconstructed 3D data had an isometric voxel size of 0.026 mm.

The study was performed using the 436.1–436.4 m depth section of cylindrical basalt core KB-01, measuring 44 mm diameter x 106 mm length (Figure 3A). However, the maximum field of view at the chosen resolution (0.026 mm) is 52 mm. Consequently, three overlapping sub-regions were scanned, reconstructed and concatenated to form the full core.

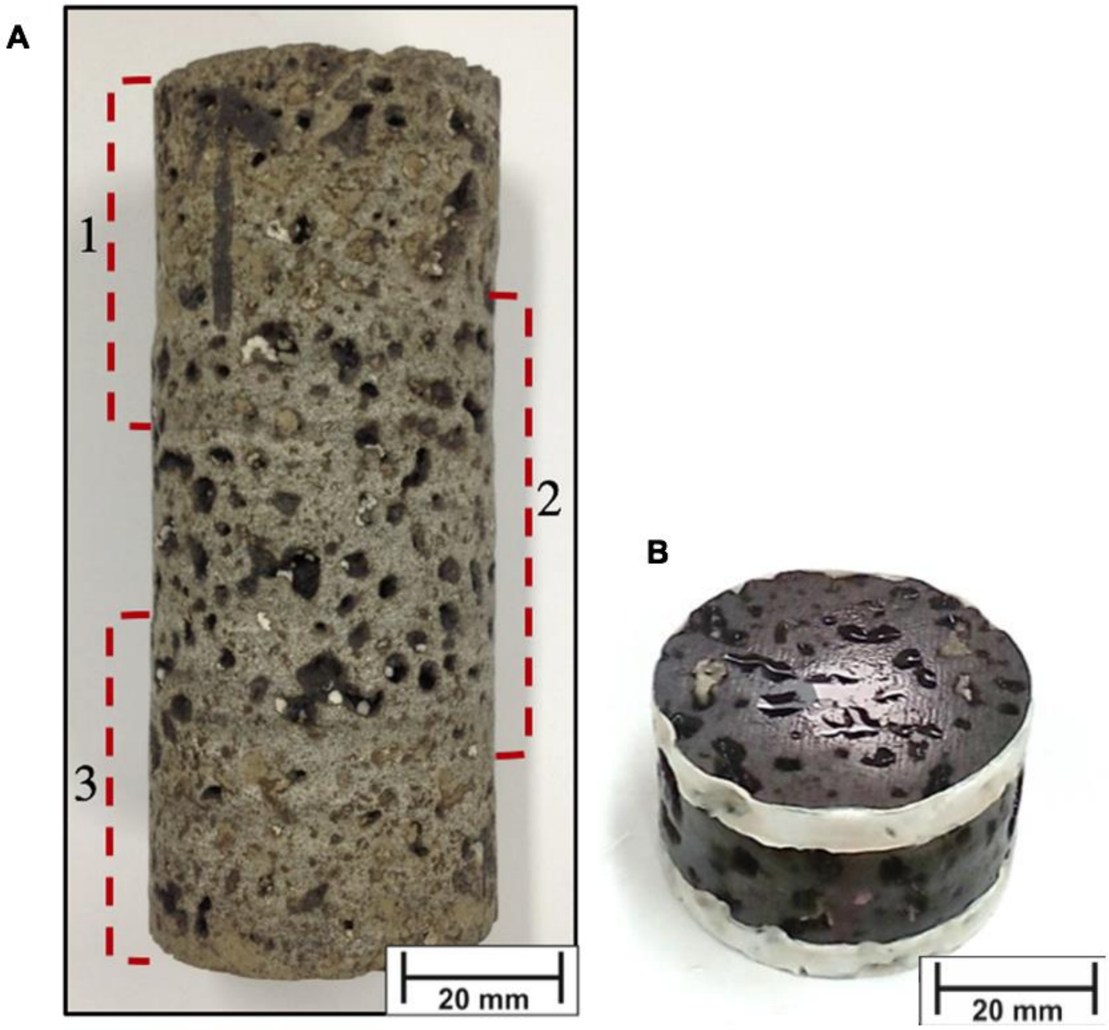

Figure 3. A Original photograph of basalt sample, KB-01, 12-1, 52-81. The dashed red lines (1-3) highlight three 52 mm length, 4.45 cm diameter overlapping sub-regions. During the 3D X-ray micro-CT (XCT) scan the sample was held vertically in place within a plastic container, suspended with

polystyrene. **B** For the hydromechanic experiment a 2.63 cm length, 4.45 cm diameter sub-sample was used, most representative of sub-region 2.

2.1.2. Volume determination

The sample volume is analysed using Avizo 9.2.0 (FEI, Oregon, USA). A region of interest (ROI) was extracted from each of the three sub-regions in order to remove edge streak noise artefacts from the data. The ROI volumes (sub-volumes) for each basalt core sub-region are shown in Table 1. Error from choosing one sub-volume ROI over another from individual core samples is negated by the fact that voids in basalt occur randomly.

Table 1. Dimensions of three region of interest (ROI) sub-volumes from basalt sample KB-01, 12-1, 52-81, from the original three overlapping sub-regions outlined in Figure 3A.

Sub-region	X (mm)	Y (mm)	Z (mm)	ROI (mm^3)
1	25.02	25.02	35.03	21928.79
2	25.00	25.00	34.85	21781.25
3	25.00	25.00	35.00	21875.00

The basalt core sample consists of two main phases: basaltic rock (mineral frame) and voids (pore space). Image processing is conducted to isolate and characterise the pore space.

The clear distinction between voids and rock (mineral frame) within the basalt sample allows a simple segmentation method to be employed. A median filter is applied to the ROI sub-volumes. The median grey level intensity value in the neighbourhood of each voxel is calculated from the results of filtering and this intensity value assigned to the output voxel (Avizo, 2016). This technique ensures the removal of white noise (scatter), a common noise artefact generated by Compton scattering, while preserving boundary edges (Ketcham and Carlson, 2001).

Binarisation is carried out, identifying the main grey-level intensity threshold of each phase, 0-15 for void space and 55-135 for rock. The grey-level intensity range separating the two phases (16-54) is assigned to one of the phases using a marker based watershed algorithm, which identifies minimum and maximum greyscale intensity variations within a region, forming the boundary between phases at maximum regional intensity variations (Figure 4) (Avizo, 2016). The method outlined ensures the removal of any partial volume effects, where boundaries between the phases in an image are blurred to an amount directly dependent on resolution size.

Following image processing, the void space diameter was validated by comparing values derived from image analysis with measurements using electronic callipers.

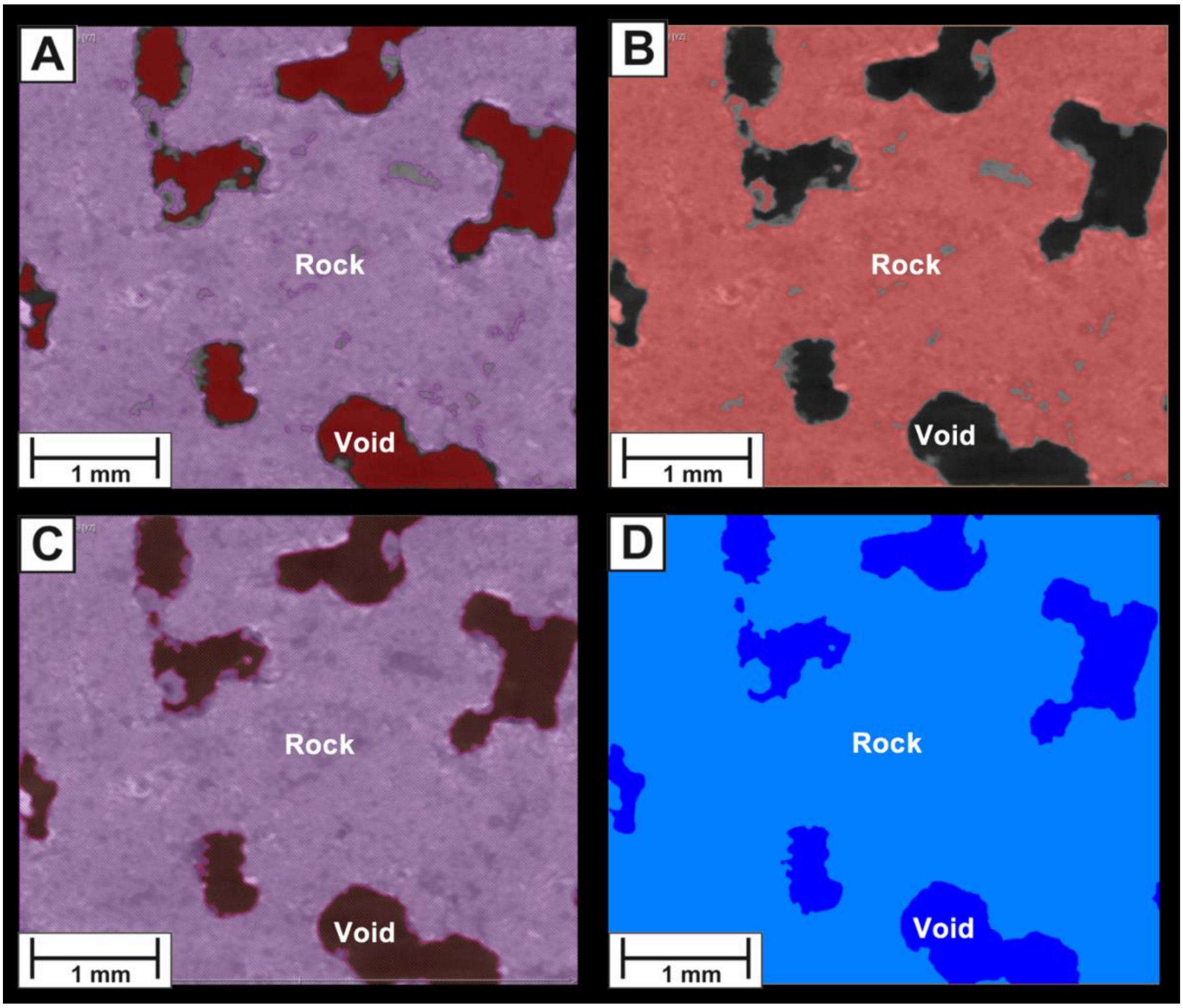

Figure 4. Orthoslice 477 in the YZ plane of region of interest (ROI) sub-volume 2 showing (**A**) The threshold range for void space, 0-15 (red) (**B**) The threshold range for rock, 55-135 (red). (**C**) The boundary between the two phases formulated using the watershed principle. (**D**) The final segmented / binarised image containing only one intensity value for void space (dark blue, 0) and one value for rock (light blue, 1).

2.1.3. Pore network model

Image processing allowed quantitative analysis of the pore space, including calculations of porosity (Equation 3) and the total specific surface area, calculated from the surface area at the interface between the pore (void) space and the rock per unit pore volume.

$$f_t = \left(\frac{V_{void}}{V_{ROI}} \right) \times 100 \tag{3}$$

where ϕ_τ is the total porosity, V_{void} is the total void space volume and V_{ROI} is the total region of interest (ROI) volume.

The connected (effective) porosity of the basalt sub-volumes was also calculated, defined as voxels assigned to the void space phase which are connected by a common face. From the connected porosity data, a pore network model was generated using a skeletonization algorithm for the pore separation process which comprises two main steps: Firstly, the algorithm uses a technique known as distance ordered homotopic thinning, which produces a one voxel thick, centred, homotopic skeleton (Youssef et al., 2007). Secondly, the pore network is partitioned into individual pore segments through analysis of the skeleton generated in the first step. The algorithm identifies maximum radii between the centred, homotopic skeleton and the contact between void space and rock in order to identify individual pore segments and throats (Youssef et al., 2007). Throats are connections between pores. A marker extent is implemented based on a qualitative assessment of the degree of segmentation to reduce the number of maximum radii and hence reduce the number of individual pore segments (Avizo, 2016). The output of the skeletonization algorithm generated a pore network, separated into 638 pores and 1144 throats.

2.1.4. Absolute permeability simulation

The vertical and horizontal absolute permeability of the connected pore network of the basalt core sub-volume geometry has been simulated using Avizo 9.2.0 software. The basis for the permeability simulation algorithm was developed by Bernard et al. (2005). The simulation solves the Navier-Stokes equation in order to determine the velocity of simulated fluid flow through the sample (Equation 4):

$$\left.\begin{aligned} \vec{\nabla}.\vec{\mathrm{V}} &= 0 \\ \mu\nabla^2\vec{\mathrm{V}} - \vec{\nabla}P &= \vec{0} \end{aligned}\right\} \tag{4}$$

where $\vec{\nabla}.$ is the divergence operator, $\vec{\nabla}$ is the gradient operator, $\vec{\mathrm{V}}$ is the velocity of the fluid simulated to flow through the porous material, μ is the dynamic viscosity of the flowing fluid, ∇^2 is the Laplacian operator and P is the pressure of the fluid simulated to flow through the porous material. Information on the parameters of the Navier-Stokes equation is sourced from Avizo (2016).

Once the Navier-Stokes equation system is solved, providing a calculation of global flow rate through the porous material, the Darcy's law equation can be applied to solve for absolute permeability (k):

$$k = \frac{mLQ}{\mathrm{D}PA} \tag{5}$$

where k is permeability, Q the volumetric flow rate through the porous material, ΔP the pressure difference applied across the sample, A the cross sectional area, L the sample length in the flow direction and μ the dynamic viscosity of the fluid.

The permeating fluid is assumed to be a single phase, incompressible and Newtonian fluid with steady-state, laminar flow conditions. To define boundary conditions, an artificial one-voxel width solid face is added to the edge of the sample face perpendicular to the main simulated flow direction. The contact between rock and void space is defined as a no-slip surface. Finally, stabilisation zones are introduced perpendicular to the main simulated flow direction to ensure that the entry and exit faces have a quasi-static pressure state.

The Kozeny-Carman equation provides an estimate of permeability from porosity and pore diameters; where pore space is defined as a random packing of spheres.

$$k_{KC} = \left(\frac{1}{180}\right)\left(\frac{\varepsilon^3}{(1-\varepsilon)^2}\right)\mathrm{d}^2 \tag{6}$$

where k_{KC} is absolute permeability, ε is the porosity of the connected void space and d is the average diameter of the spheres. The equation will be used to validate results obtained from the simulation, in addition to those from the hydromechanical experiments.

2.2. Hydromechanical test

2.2.1. Sample preparation

The hydromechanical test was performed on a 26.3 mm long, 44.5 mm diameter sample extracted from sample KB-01, 12-1, 52-81, sub-region 2 (Figure

3B). The sample was cut and ground in parallel within ± 0.01 mm from the original specimen. The sample has a dry density of 2412 kg m^{-3}.

The sample was equipped with a 90° bi-axial set of 350 Ohm electrical strain gauges, epoxy-glued on the lateral side of the sample, to record axial and radial strains related to stress variations during the tests. The sample was saturated in a degassed 35 g L^{-1} NaCl (synthetic) brine via water imbibition in a vacuum vessel prior to the experiments (Amalokwu et al., 2014). The porosity (ϕ) was estimated as 26.2 %, determined by dry to brine-saturated weight difference.

2.2.2. Experimental setup

The test was performed using a modified experimental setup of that presented in Falcon-Suarez et al. (2016), shown in Figure 5.

The sample is housed in a triaxial cell core holder that allows pressurising rock samples up to 65 MPa of confining (axial, σ_1, and radial, $\sigma_2= \sigma_3$, independently) and pore pressure. The confining fluid (mineral oil) is delivered from a dual pumping controller (Teledyne ISCO model EX100D), configured in a hydrostatic mode (i.e., confining pressure $P_c= \sigma_1= \sigma_2= \sigma_3$) for the experiment. Inside the vessel, the rubber sleeve that isolates the core plug from the confining fluid is equipped with 16 stainless steel electrodes which, once in contact with the sample, provide electrical resistivity tomography measurements (North et al., 2013). Under typical operating conditions the resistivity measurement error is ~5 % for samples in the electrical resistivity range 1 - 100 Ω m.

The two platens that apply axial stress to the sample have inlet and outlet ports to conduct the pore fluid through the sample. The platens are configured to bypass the leads from strain gauges added on the side-wall of the rock sample. The leads are connected to a four channel strains data acquisition system (Vishay-Model D4). The pore pressure is also servo-controlled by two delivery and one receiver high pressure, high accuracy, pumping controllers. To further control the pore pressure, two piezo-resistive pressure transmitters (Keller model PA-33X) are located in the pipeline, up- and downstream of the sample, to accurately measure pressure drops and temperature changes during the test. The pore fluids are supplied indirectly via fluid transfer vessels (FTVs) with the aim of preventing potential damage to the controllers from corrosive fluids, such as the 35 g L^{-1} synthetic brine used for the test (Falcon-Suarez et al., 2016).

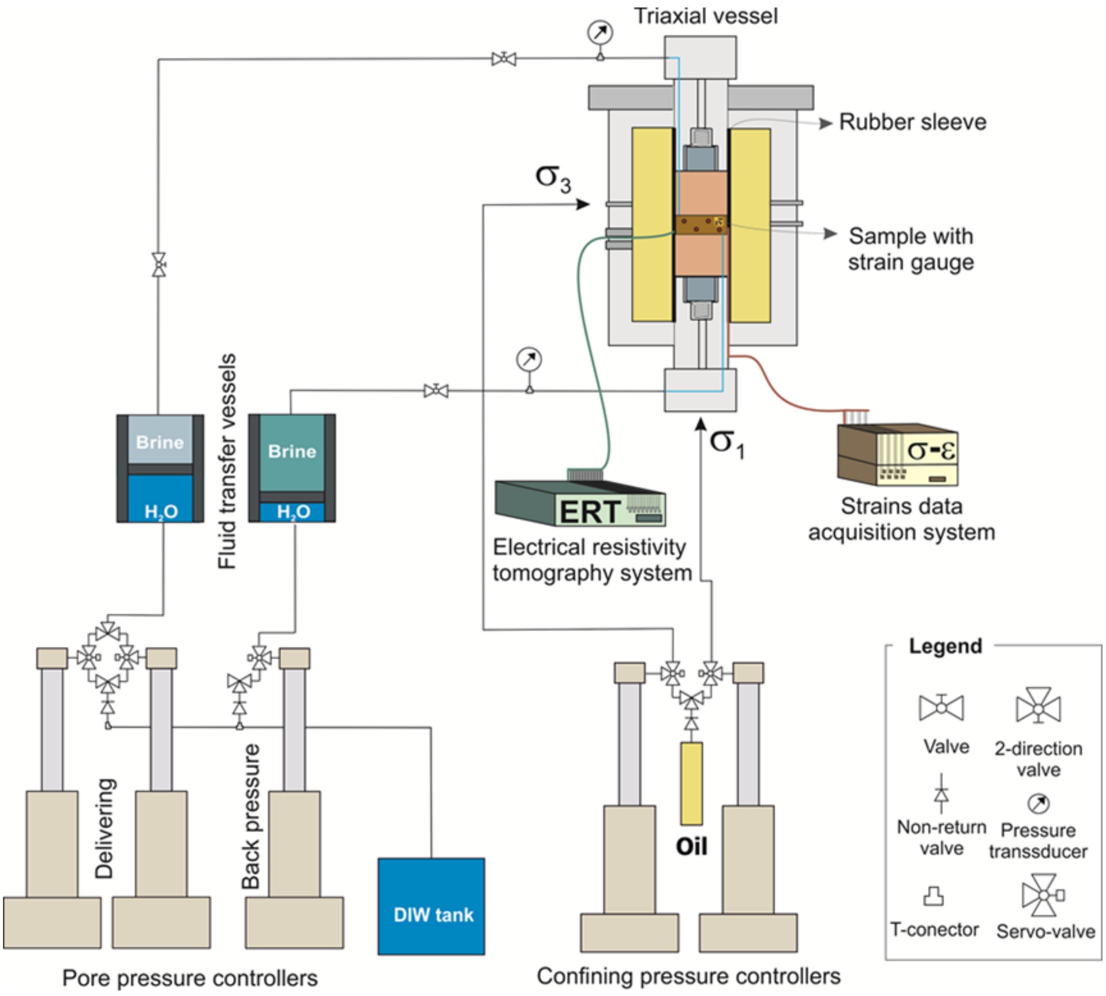

Figure 5. The rock mechanics experimental rig set up, comprised of: A triaxial vessel with rubber sleeve and platens, confining pressure controllers, electrical resistivity tomography system, strains

data acquisition system, pore pressure controllers, piezo-resistive pressure transmitters and fluid transfer vessels. See text for detailed description.

2.2.3. Test methodology

Fluid distribution in reservoirs is ultimately controlled by permeability, which is a pressure dependent parameter (Fisher, 1998). To investigate the dependency of the permeability of the basalt sample to confining (P_c) and pore pressures (P_p), a loading/unloading differential stress path was configured to simulate variable shallow conditions (~400 m depth under oceanic crust), between 1 - 7 MPa of differential pressure ($P_{diff} = P_c - P_p$). Two tests were subsequently conducted under the defined differential stress conditions to investigate (i) variations of transport properties through the monitoring of permeability and electrical resistivity, representative of the pore connectivity (Berryman, 1992), and (ii) to determine the resultant volumetric deformation of the rock sample.

The stress-strain test was conducted under drained hydrostatic conditions and repeated twice, varying slightly the loading rate (from 0.02 to 0.05 MPa s^{-1}) to investigate hysteresis effects in the volumetric strain recovery. From the axial and radial strains (ε_a and ε_r, respectively), volumetric strain (ε_v) was calculated as $\varepsilon_v = \varepsilon_a + 2\varepsilon_r$, which reflects porosity variations ($\Delta\phi$) in the sample.

Permeability of brine was determined using the steady state flow method, applying Darcy´s law. The test was performed by setting constant the pressure upstream of the sample while monitoring the pressure gradient and the flow rate up and downstream, until steady state was achieved for each P_{diff} stage. Permeability and electrical resistivity were measured three times per P_{diff} along the stress path.

3. Results

3.1. X-Ray micro-CT results

3.1.1. Porosity workflow

The results of quantitative analysis of the pore space performed on the filtered and segmented basalt sample sub-volume (Figure 6A) are summarised in Table 2.

Table 2. Results for the total and connected porosity, specific surface area and connected porosity as a percentage of total porosity for the three sub-region sub-volumes outlined in Table 1.

Sub-volume	$\phi\tau$ (%)	$Ss\tau$ (mm^{-1})	$\phi\chi$ (%)	$Ss\chi$ (mm^{-1})	$\phi\chi/\phi\tau$ (%)
1	10.99	0.45	2.05	0.10	18.70
2	15.23	0.46	8.76	0.33	57.50
3	17.10	0.57	3.80	0.13	22.20

$\phi\tau$ and $\phi\chi$ are total and connected porosity respectively, Ss is specific surface area; subindices τ and χ are for total and connected pores respectively.

Connected porosity is a more significant parameter to the study than total porosity because isolated pores would not allow permeation of CO_2 injection fluid (Figure 6C). Thus isolated pores should be omitted from calculations of total CO_2 reservoir storage capacity. The connected porosity ranges from 2.05–8.76 %. The sub-volumes display a large range of connected porosity as a percentage of total porosity, ranging from 18.7–57.5 %. It appears that a higher total porosity does not correlate directly with a larger connected porosity.

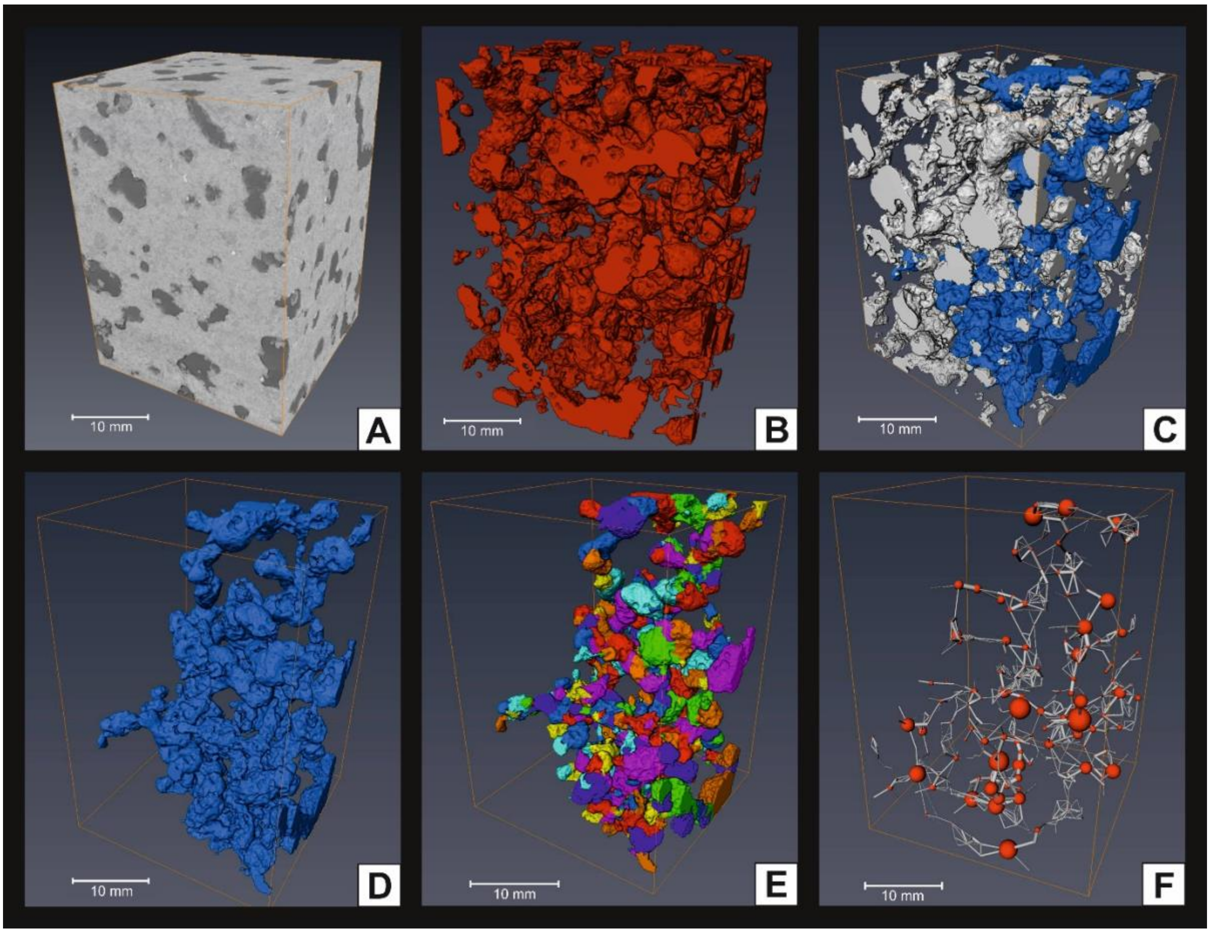

Figure 6. Volume rendering of the cropped ROI sub-volume (region of interest) of basalt sub-region 2, displaying: (**A**) Original grey-level intensity (**B**) Total porosity (red) (**C**) Effective / connected porosity (blue) and isolated porosity (white) (**D**) Connected (effective) porosity (blue) (**E**) Pore separation of connected pore space, 638 pores were defined and (**F**) Pore network model of the pores (red) and throats /pore connections (grey) on a scale which shows relative pore volume size (scale factor of 3.3E-8) and relative throat equivalent radii (scale factor 0.15). A total of 1144 throats were defined. See supplementary material in online version for video animations.

3.1.2. Connected pore network model statistics

This section focuses on the connected pore statistics of basalt core sub-volume 2, however the same distributions of each statistical parameter were observed in sub-volumes 1 and 3.

Figure 7A shows a frequency distribution plot of pore surface area in contact with rock per unit pore volume, which provides a reactive surface for carbonate precipitation. The surface area ranges from 0.006 mm^{-1} up to 83 mm^{-1}. The graph shows an exponential decrease in frequency with increased surface area.

Figure 7B shows a frequency distribution plot of coordination number (*CN*), defined as the number of throats connecting each pore segment to adjacent pore segments. The *CN* ranges from 1 up to a maximum of 17. A *CN* of 2 defines a pore segment with only one entry point and one exit point for permeating fluid, while a *CN* of 1 indicates a termination pore. The plot has a log-normal frequency distribution, with a value of 2 being the most common coordination number.

Figure 7C shows a frequency distribution plot of pore radii and throat radii. Pore radius is defined as the radius of an equivalent spherical pore with the same volume. The values of pore radii and throat radii are very similar, both parameters have a log-normal frequency distribution. Pore radii and throat radii have a very similar size range, from 0.02–2 mm and 0.01–2 mm respectively, as well as the same modal value of ~0.25 mm. The only subtle difference between the two parameters is that throat radii have a slightly more non-uniform distribution across the range, with a greater frequency distribution of throat radii <0.65 mm.

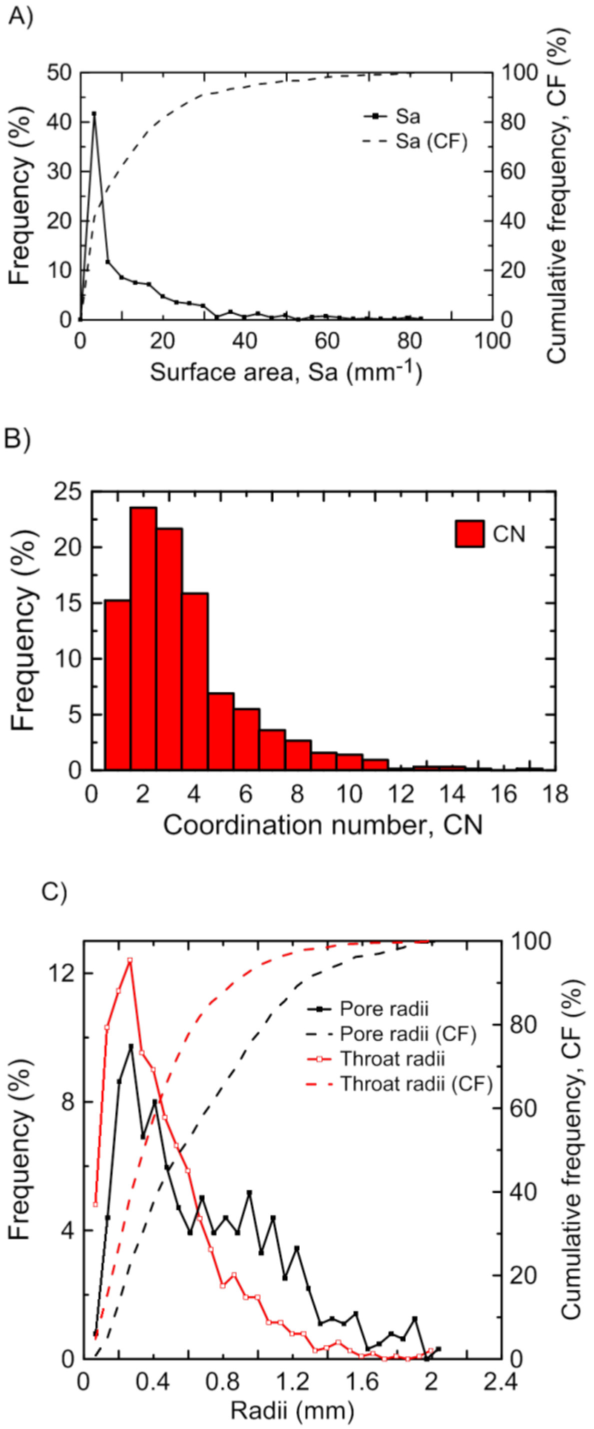

Figure 7. Pore statistics generated from a pore network model of 638 defined pore segments and 1144 throats (connections between pores) for basalt ROI (region of interest) sub-volume 2.**A.** Frequency distribution plot of pore surface area in contact with rock (mm^{-1}). The distribution has been plotted into 25 equally spaced bin intervals of 3.3 mm^{-1} across the full range. **B.** Log normal frequency distribution plot of coordination number. **C.** Log-normal frequency distribution of pore radii (blue) and throat radii (red). Both parameters have been plotted into 30 equally spaced intervals of ~ 0.07 mm across the full range.

3.1.3. Absolute permeability simulation

The input parameters of the vertical and horizontal absolute permeability simulations of basalt sub-volume 2 are described in Table 3. In addition, the results of the vertical and horizontal absolute permeability simulation of basalt sub-volume 2 are described in Table 4.

Table 3. The input parameters of the simulation used to calculate the vertical (Z-axis) and horizontal (X-axis) absolute permeability (k) of basalt sub-volume 2.

Plane	A (m^2)	μ (Pa.s)	P_{in} (Pa)	P_{out} (Pa)	ΔP (Pa)	L (m)	Iter.
Vertical	6.25×10^{-4}	0.001	130000	100000	30000	0.035	40620
Horizontal	8.71×10^{-4}	0.001	130000	100000	30000	0.025	76500

A is cross sectional area, μ the dynamic viscosity of the fluid, P_{in} the input pressure, P_{out} the output pressure, ΔP the pressure difference applied across the sample, L the sample length in the flow direction and Iter. the number of iterations the simulation was run.

Table 4. The output values of the simulation used to calculate the vertical (Z-axis) and horizontal (X-axis) absolute permeability (k) of basalt sub-volume 2.

Plane	k (m^2)	Q (m^3s^{-1})	Error (%)	Simulation time
Vertical	2.07×10^{-10}	9.7969×10^{-5}	0.01	2.5 days
Horizontal	5.10×10^{-11}	5.0832×10^{-5}	0.00241	4.75 days

K is absolute permeability and Q is the average flow rate of the simulated fluid.

From the simulation a vertical absolute permeability of 2.07×10^{-10} m^2 and a horizontal absolute permeability of 5.10×10^{-11} m^2 are obtained (Figure 8). The horizontal permeability (5.10×10^{-11} m^2) is simulated as one order of magnitude less than the vertical absolute permeability (2.07×10^{-10} m^2).

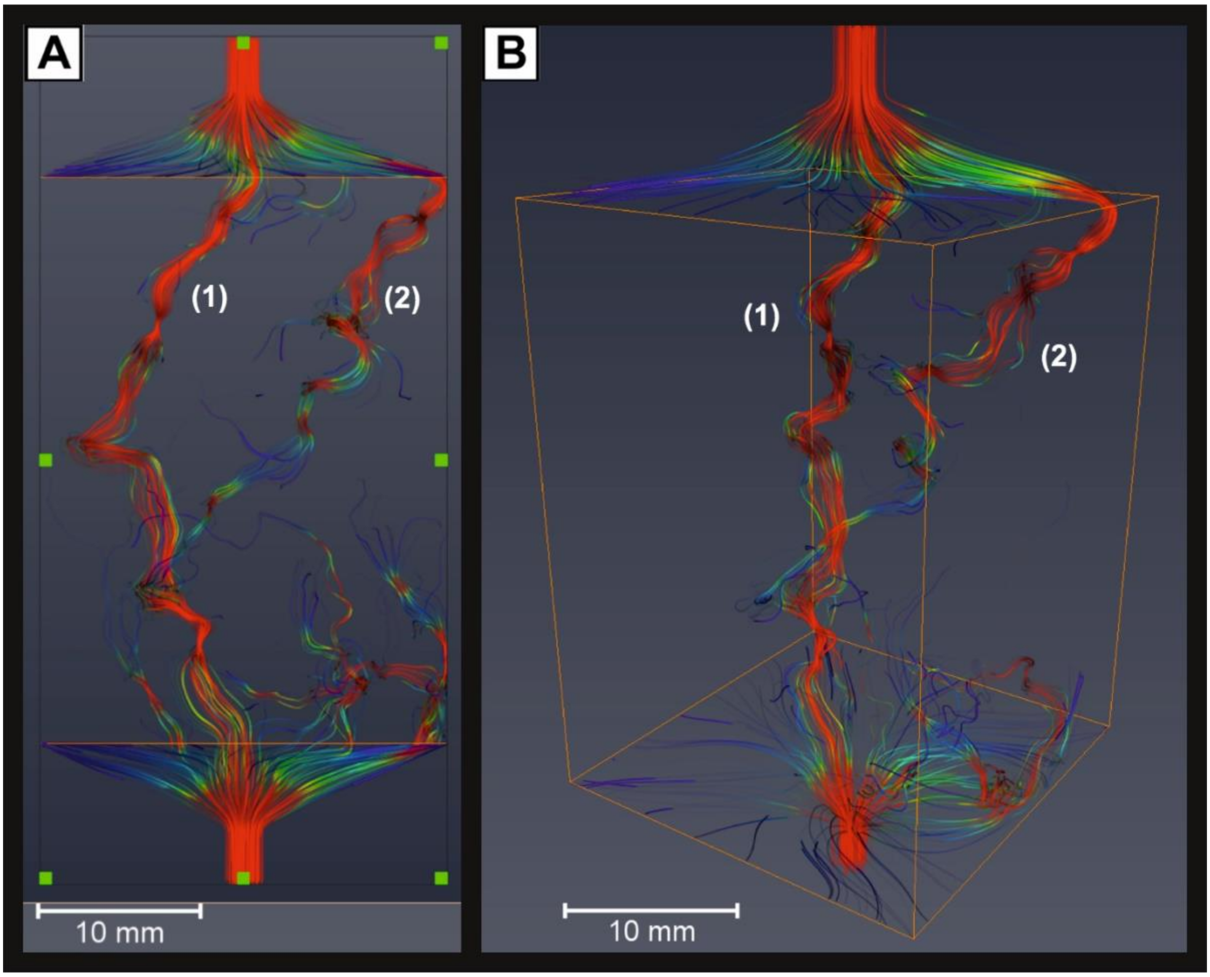

Figure 8. Volume rendering illustration image of the velocity field model from the vertical absolute permeability simulation. The colourmap displays areas of higher velocity fluid flow in red and lower velocity flow in blue. (**A**) Experimental setups are shown, equating to 25 % additional sample length, perpendicular to the main simulated flow direction to ensure the entry face has a quasi-static pressure state. (**B**) 3D view of the velocity field model. The velocity field model appears to show two main fluid flow pathways (1) and (2).

3.1.4. Permeability validation using the Kozeny-Carman equation

Permeability calculated using Equation 6 is summarised in Table 5. The mean value obtained (7.7 x10^{-12} m^2) is one order of magnitude less than the simulated horizontal permeability, whilst the maximum value (7.4 x10^{-11} m^2) is synonymous with the horizontal permeability. Thus it may be reasonable to use the Kozeny-Carman equation to validate the absolute permeability values obtained from the simulation. To further validate the absolute permeability values, the results of rock mechanics experiments are shown in the next section.

Table 5. The absolute permeability (k) is calculated using the Kozeny-Carman equation (Equation 6). The equation provides an estimate of permeability from the pore diameters and connected porosity of basalt sub-volume 2.

	D_{pore} (m)	k (m^2)
Min.	4.69×10^{-5}	1.0×10^{-14}
Mean	1.31×10^{-3}	7.7×10^{-12}
Max.	4.07×10^{-3}	7.4×10^{-11}

D_{pore} is pore (sphere) diameters obtained from twice the value of pore radii, obtained from pore statistics of 638 defined pore segments for basalt sub-volume 2.

3.2. Hydromechanical test results

The variation of strain, porosity, electrical resistivity and permeability with applied differential stress during the hydromechanical test, conducted on the basalt sample is shown in Figure 9. Stress loading leads to porosity decrease, which directly affects permeability and inversely affects the electrical resistivity as pore volume decreases.

As a preliminary step, permeability was calculated under atmospheric (unconfined) conditions, resulting in ~1.56 Darcy (D) (~10^{-12} m^2). This value decreases by one order of magnitude (~10^{-13} m^2) with initial loading (P_{diff} = 1 MPa), but up to three orders of magnitude (~10^{-15} m^2) at maximum differential stress (P_{diff} = 7 MPa). Confining pressure principally affects the value of permeability. At constant differential stress (P_{diff} = 4 MPa), a lower permeability is observed at a higher confining pressure (9 MPa compared to 6 MPa) (Figure 9).

At a maximum sample compression of 7 MPa, a volumetric deformation (ε_v) of ~0.025 % is observed. At 4 MPa, most equivalent to the original reservoir conditions of the basalt sample at ~400 m depth, a volumetric deformation of ~0.0125 % is observed.

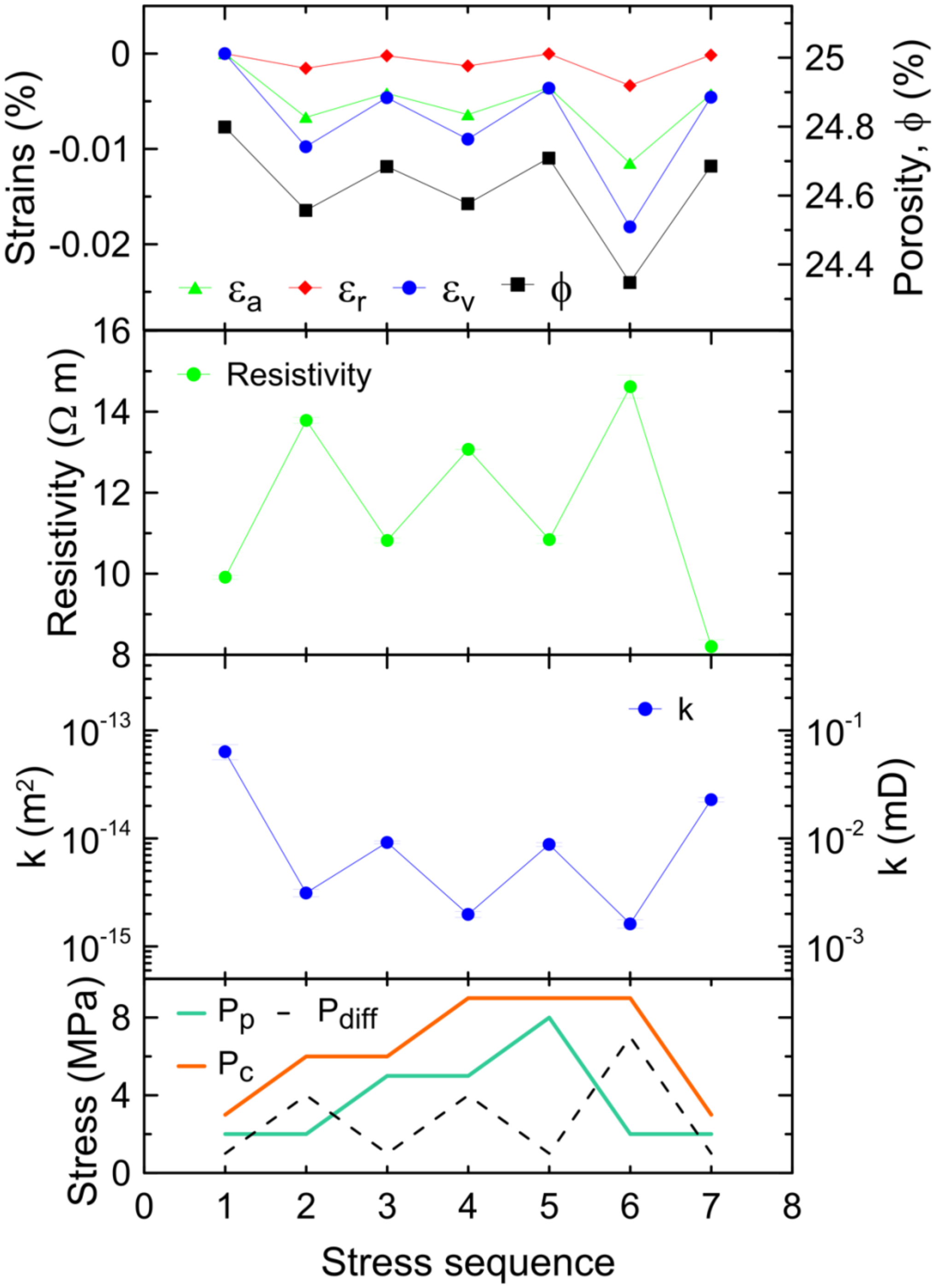

Figure 9. Strains (ε_a, ε_r and ε_v), porosity (ϕ), electrical resistivity and permeability (k) for each state of stress (P_{diff}). ε_a, ε_r and ε_v are axial, radial and volumetric deformations, respectively. P_c, P_p and P_{diff} are confining, pore and differential pressures respectively.

4. Discussion

4.1. Pore network model of basalt

Initial (total) porosity of basalt lava flows ranges between 5–40 % (Franzson et al., 2008). Geochemical alteration of basalts, causing secondary mineralisation in pore space, reduces porosity to ~1–10 % (Sigurdsson and Stefánsson, 1994). At the CarbFix site, the connected porosity of the basalt estimated from hydrological models, pump tests and tracer tests is ~8.5 % (Aradóttir et al., 2012). Total porosities determined from XCT image analysis of basalt of 11.0–17.1 % and connected porosities of 2.05–8.76 % are in strong agreement with the results of field scale testing. The connected porosity as a percentage of total porosity varied from 18.7 % up to 57.5 % of total porosity, reflective of basalt heterogeneity.

The porosity value determined from a dry-wet weight difference of 26.2 % was 9.1 % greater than the maximum value obtained by the XCT image analysis. This may lead to the interpretation that there is an intergranular micropore network and / or microcracks that have not been characterised in this particular study, as they would occur at sub-voxel (<26 µm) resolution (Leu et al., 2014). The increased experimentally-derived porosity may also be due to stress-release induced microcracking focused at the sample margins, created during the initial coring and extraction of the sample at the CarbFix site. The central parts of the sample, where the image analysis was focused, are less likely to incur damage than the external parts of the plug, which would have been more exposed to the action of the mechanical tools for coring and sample preparation. In this line, the results of the stress-strain test indicate that the sample behaves (quasi) elastically for the differential stress path adopted in the experiment. However, minor hysteresis of the permeability, resistivity and strains recovery was observed from the first to the second loading cycle, likely related to the presence of microcracks that close during initial loading stages. The interpretation of micropores (intergranular porosity) and microcracks has been omitted from CO_2 sequestration potential calculations, as the permeability and reactive surface area may not be deemed high enough for carbonate precipitation.

4.2. X-Ray micro-CT revised results following the hydromechanical test

During the hydromechanical test, permeabiltiy decreased by three orders of magnitude (10^{-14} m^2) from atmospheric (unconfined) to reservoir conditions (P_{diff} = 4 MPa at ~400 m depth). The magnitude of the volumetric deformation (strain) ranged from 0.01 to 0.02 %, which is equivalent to 2.5–5 µm pore diameter reduction, assuming isotropic stress-strain conditions (Equation 7):

$$D_{R} = D_{X}(1 - \Delta\varepsilon) \tag{7}$$

where $\Delta\varepsilon$ is the strain, D_X and D_R are the sample diameters before and after applying the strain respectively.

To further analyse whether the pore diameter reduction is the primary cause of the observed permeability decrease in the hydromechanical experiments, the pore geometry aquired using XCT was modified to reduce the originally calculated pore diameters in further XCT image-based simulations (Figure 10). The procedure consisted of applying the erosion tool incorporated in Avizo to the binarised image of rock and void space. The tool reduces the void space of the connected pore network channel by one voxel width (equivalent to 52.4 µm), which artificially simulates the effect of pore diameter reduction under confining pressure. A 52.4 µm reduction of pore diameter is equivalent to >10 times the deformation observed from the hydromechanical strain analysis (2.5–5 µm). However, artificially reducing the pore diameter by 52.4 µm using the XCT image-based simulation will account for volumetric deformation that may have been undetected by the strain gauges, which were epoxy-glued on the lateral side of the sample, if deformation took place under non-isotropic stress-strain conditions. A complete pore flow pathway closure of ≥ 66 µm is unlikely to be representative of true stress-strain conditions, so has not been addressed in this study.

As shown in Table 6, absolute vertical permeability (k_v) decreases by less than one order of magnitude (1.89 x10^{-10} m^2) when a 52.4 µm reduction in pore diameter is applied to an image-based simulation. This is in stark contrast with the three orders of magnitude (10^{-14} m^2) decrease seen in the hydromechanical experiments. This anomaly suggests that additional mechanisms, besides from pore diameter reduction, are causing the significant permeability decrease in the hydromechanical tests (refer to Chapter 4.5. of Discussion).

Table 6. The effect on the pore reservoir properties of basalt sub-volume 2, following a reduction in pore diameter by 52.4 µm in an image-based simulation.

	$\phi\chi$ (%)	$Ss\chi$ (mm^{-1})	k_v (m^2)	Min. D_{throat} (µm)	Max. D_{throat} (µm)
Value before pore diameter reduction	8.76	0.33	2.07×10^{-10}	66.43	1993.02
Value after pore diameter reduction	7.86	0.23	1.89×10^{-10}	14.03	1940.62
Percentage reduction (%)	0.90	29.10	8.60	78.90	2.60

$\phi\chi$ is connected porosity, $Ss\chi$ is specific surface area of connected pores, k_v is absolute vertical permeability, Min. and Max. D_{throat} are the minimum and maximum pore throat diameters respectively.

4.3. Absolute permeability of basalt

Saar and Manga (1999) reported absolute permeability (k) values in the range 10^{-9}–10^{-14} m^2 for vesicular basalts, in agreement with bulk permeability estimates of young oceanic crust in a shallow basement proposed by Fisher (1998) in the range of 10^{-9}–10^{-13} m^2, increasing with depth.

Two and three dimensional field scale basalt reservoir models of the CarbFix site have reported horizontal and vertical absolute permeabilities (k_h and k_v) of 3.0 x10^{-13} m^2 and 1.7 x10^{-12} m^2 respectively (Aradóttir et al., 2012). Absolute permeability simulations, performed on geometry acquired using XCT, resulted in horizontal and vertical absolute permeabilities (k_h and k_v) of 5.10 x10^{-11} m^2 and 2.07 x10^{-10} m^2 respectively, which lie within the expected range for basalt. The vertical absolute permeability was one order of magnitude greater than the simulated horizontal permeability, which was expected from field scale models. Aradóttir et al. (2012) suggested that the increased vertical permeability is due to the presence of vertical basalt columns, surrounded by a sub-vertical fracture network. From evidence obtained from XCT image analysis, the increased vertical permeability may be interpreted to be due to the orientation of the sub-vertical branching pore network. Joints may form in basalt flows due to tensional stress produced by differential cooling rates of a single lava flow (McGrail et al., 2006). One hypothesis is that the differential cooling rate responsible for the formation of joints may also be responsible for the formation of the vertical branching network of coalesced vesicles. A differential cooling rate would be exacerbated in lava flows forming beneath a glacier, expected in this region (Schopka et al., 2006).

The permeability values (k_h and k_v) of the basalt reservoir field scale models outlined in the previous paragraph were up to two orders of magnitude less than values obtained using XCT image analysis. The spatial extent of the connectivity of the vertical branching network of coalesced vesicles on a kilometre reservoir scale may differ from that of a centimetre core scale, making the validity of the permeability values obtained from simulations using XCT image analysis questionable. The core scale studies may miss larger flow paths, for example at the top and bottom of lava flows. The 150 m of core extracted from the basalt storage reservoir represents <1.6 x10^{-8} % of the total reservoir volume, supporting the idea that representative sampling is a limitation of the study. However, this limitation applies to any reservoir study on a laboratory scale.

4.4. CO_2 sequestration potential of basalt

From XCT image analysis of the basalt core sample, an estimated 0.33 Gt of CO_2 can be sequestered in the basalt storage formation at the CarbFix site (Table 7). The estimate of CO_2 in situ mineral carbonation potential is based upon calculations of connected porosity and reactive surface area from XCT analysis, combined with volume calculations of the basalt storage formation and calculations of mineral carbonation CO_2 fixation per unit surface area from Aradóttir et al. (2012). The volume of the basalt storage reservoir formation was calculated from the average thickness of the formation (0.4km), multiplied by an approximate length (2.5 km) and width (1.8 km) of the CarbFix site.

Table 7. Calculation of the total CO_2 sequestration potential, in Gigatonnes of CO_2, of the basalt storage formation at the CarbFix site.

	$\phi\chi$	$Ss\chi$ (km^{-1})	Volume of basalt storage formation (km^3)	Mineral carbonation CO_2 fixation per unit surface area (Gt CO_2/ km^2)	Total CO_2 sequestration potential (Gt CO_2)
Min.	0.0205	1.0×10^5	1.8	5.0×10^{-6}	0.018
Mean.	0.0487	1.9×10^5	1.8	2.0×10^{-5}	0.33
Max.	0.0876	3.3×10^5	1.8	3.5×10^{-5}	1.82

Values of connected porosity $\phi\chi$ and reactive surface area of connected pores $Ss\chi$ were obtained from X-Ray micro-CT (XCT) image analysis of basalt core. Values for the volume of the basalt storage formation and estimated mineral carbonation CO_2 fixation per unit surface area are taken from Aradóttir et al. (2012). The total CO_2 sequestration potential is calculated by multiplying the four values together.

Theoretically, if CO_2 sequestration is applied along the entire length of the active rift zone in Iceland, an estimated 6100 Gt CO_2 could be sequestered (Table 8, using mean values of connected porosity, reactive surface area and mineral carbonation CO_2 fixation per unit surface area from Table 7), which is in agreement with upper estimates of 7000 Gt CO_2 by Snæbjörnsdóttir and Gislason (2016). The estimate relies on the assumption that basalt formations along the area of the active rift zone in Iceland have similar porosities and reactive surface areas as the storage formation at the CarbFix site, based on their similar age of formation and hence similar degree of alteration.

Table 8. An estimation of the total CO_2 sequestration potential, in Gigatonnes of CO_2, along the active rift zone in Iceland, using the calculated values of connected porosity and reactive surface area of basalt from the study. The mean value is 6100 Gt CO_2, ranging from a minimum of 2600 Gt CO_2 to a maximum of 33400 Gt CO_2.

	Length (km)	Average Width (km)	Area (km^2)	Average thickness of basalt sequence (km)	Total CO_2 sequestration potential (Gt CO_2)
Active rift zone in Iceland	600	55	33000	1	6100
					2600 to 33400

The average thickness of the basalt sequence along the rift zone has been estimated to have the same thickness as the basalt storage formation at the CarbFix site (1 km). The dimensions of the active rift zone in Iceland are taken from Snæbjörnsdóttir et al. (2014), outlined in red on a map of Iceland in Figure 1B.

For comparison, the total anthropogenic CO_2 release to the atmosphere from fossil fuels, cement production and land use change is estimated at 39.6 Gt CO_2 per year (Le Quéré et al., 2016). The upper estimate of CO_2 sequestration potential along the active rift zone in Iceland of 33400 Gt CO_2 (Table 8), using maximum calculated values of connected porosity, reactive surface area and mineral carbonation CO_2 fixation per unit surface area (Table 7) is greater than the total CO_2 emissions estimated from the burning of all fossil fuel on Earth, estimated at 18500 Gt CO_2 (Archer, 2005).

4.5. Pore space clogging in basalt

Two main observations suggest that pore clogging could be a major concern for CO_2 storage in basalt. Firstly, a modal coordination number (pore connectivity) of 2 was found, implying predominantly one fluid flow entry point and exit pathway through pores. Secondly, an exponential decrease in pore surface area frequency distribution was observed. The frequency distribution implies that the majority of pore segments (>40 %) have a low surface area <5 mm^{-1}. Pore segments <5 mm^{-1} in surface area are likely to be highly prone to clogging (Figure 10). If clogging takes place, the total connected reservoir volume would be reduced, and consequently the calculated CO_2 sequestration potential of the basalt reservoir may be overestimated.

Differences of up to four orders of magnitude in permeability were found between the XCT simulations (~10^{-10} m^2) and the hydromechanical tests (~10^{-14} m^2) at realistic reservoir confining pressures. Revised XCT permeability simulations with a reduced pore network diameter, to replicate the effect of compression under reservoir confining pressures, lead to a minor permeability decrease of ~8.6% (1.89 x10^{-10} m^2). Therefore, pore volume reduction at higher confining pressures seems to be insufficient to explain the permeability reduction observed during the hydromechanical tests.

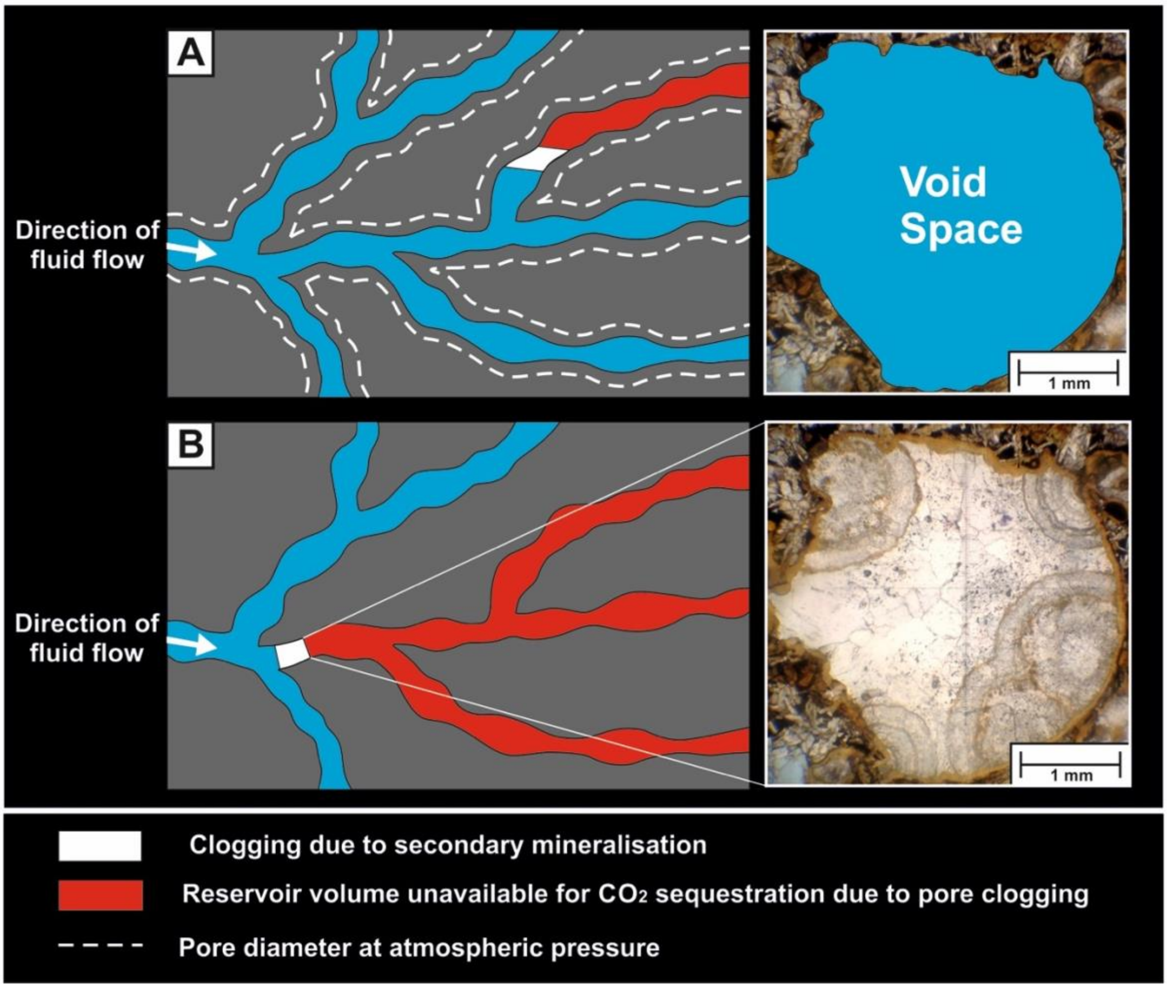

Figure 10. A schematic diagram showing a branching network of connected void space (blue). The clogging of one pore segment with a coordination number (pore connectivity) of 2 would cause a blockage in the pore network, potentially isolating void space formerly connected to the network. Clogging in scenarios (**A**) and (**B**) would have an incrementally greater effect on the basalt reservoir connected pore volume and hence a reduction in CO_2 sequestration potential of the reservoir. In (**A**) the white dashed line represents schematically the size of the pore diameter prior to the addition of confining pressure, represented artificially by the erosion tool in further X-Ray micro-CT simulations.

One hypothesis for such a significant permeability reduction is from clay swelling effects. Smectite is one of the most abundant types of swelling clays present in basaltic rocks (Schiffman and Fridleifsson, 1991). From the work of Alfredsson et al. (2013), smectite clays are expected to be present at the depth the core sample was extracted (~436 m depth). Smectite, in addition to other clay minerals, were found to be supersaturated in HN-04 well water samples, supporting evidence for their abundance within the void space (Snæbjörnsdóttir et al., 2017). Importantly, smectite can create an impermeable barrier to fluid flow when located in large pore space, represented by the coalesced vesicles (Aksu et al., 2015). Secondary precipitation effects on the reduction of porosity/permeability in basalt has been further analysed by Franzson et al. (2008), who proposed that the amount of clay precipitation infilling vesicles is inversely proportional to porosity/permeability. The amount of clay precipitation is also found to increase with the age of oceanic basalt, as alteration progresses (Fisher, 1998).

Furthermore, the clay swelling effect becomes exacerbated in high salinity fluids, such as those used in the hydromechanical tests (i.e. 35 g L^{-1} NaCl-brine). The changing ionic conditions caused by the seawater-like pore fluid, may have triggered the remobilisation of clay from the pore walls, creating pore blockage (Amorim et al., 2007; Mohan et al., 1993). It has been strongly proposed that high salinity seawater may be used for future, cost-effective upscaling of CO_2 injection, for both onshore and offshore basaltic reservoirs (Goldberg and Slagle, 2009; Goldberg et al., 2010; Snaebjornsdottir and Gislason, 2016; Wolff-Boenisch et al., 2011). Therefore, clay swelling and remobilisation are important mechanisms that require further investigation, to assess the effect this process has on the CO_2 sequestration potential of a basalt reservoir. Without further study into the effects of clay swelling, remobilisation and pore blockage, which becomes exacerbated in high salinity fluids, CO_2 storage in basalt may be restricted to sites with fresh water available for CO_2 injection and areas of fresh basalts with a low percentage of clay precipitated in the pore space.

5. Conclusions

3D X-Ray micro-CT (XCT) image analysis together with hydromechanical experiments at realistic reservoir conditions were combined to investigate transport properties and storage capacity of the basaltic reservoir formations at the CarbFix site in Iceland. This study provides important benchmark data for the future upscaling and optimisation of CO_2 storage in continental and ocean crust basalt formation.

The main findings of the study are:

- A larger absolute vertical permeability of basalt relative to horizontal permeability is observed, due to a sub-vertical branching vesicle network interpreted to have formed because of differential cooling rates of a basaltic lava flow.

- Estimates suggest a basalt reservoir CO_2 sequestration potential of 0.33 Gt CO_2 at the CarbFix site (Iceland), with an estimated CO_2 sequestration potential along the active rift zone in Iceland of 6100 Gt CO_2.
- Processes of pore clogging created by carbonate mineral precipitation and clay swelling should be the focus of further studies to better constrain the CO_2 sequestration potential of basalt.

Acknowledgments

We acknowledge funding from U.S. Department of Energy under award number DE-FE0004847 for core drilling and from Southampton Marine and Maritime Institute (SMMI) for core sample collection and characterisation. This project has also received funding from the European Union’s Horizon 2020 research and innovation programme under grant agreement No. 654462 - STEMM-CCS. We would like to thank our colleagues Sandra Ó. Snæbjörnsdóttir and Annette K. Mortensen at Reykjavik Energy, Helga Margrét Helgadóttir at Iceland GeoSurvey and Michelle Harris at University of Plymouth for their contribution to the core characterisation during and after the drilling of KB-01. We are also indebted to Edda Sif Aradottir (Reykjavik Energy), Eric H. Oelkers (CNRS/UMR Toulouse, France), Sigurdur R. Gislason (University of Iceland), Martin Stute and Wallace Broecker (Lamont-Doherty Earth Observatory, Columbia University, USA), Hólmfriđur Sigurđadottir, Einar Gunnlaugsson, Bergur Sigfússon and Ingvi Gunnarsson at Reykjavik Energy for their overall contributions to the CarbFix project. We would also like to thank our colleagues at the µ-VIS X-Ray Imaging Centre, University of Southampton for use of their high resolution X-Ray computed tomography (CT) facilities and image processing suite, including their helpful advice and support. Finally, we would like to thank the FEI Visualization Sciences Group for providing the use of the Avizo 9.2.0 software for X-Ray micro-CT (XCT) image processing.

References

Aksu, I., Bazilevskaya, E., Karpyn, Z.T., 2015. Swelling of clay minerals in unconsolidated porous media and its impact on permeability. GeoResJ 7, 1-13.

Alfredsson, H.A., Oelkers, E.H., Hardarsson, B.S., Franzson, H., Gunnlaugsson, E., Gislason, S.R., 2013. The geology and water chemistry of the Hellisheidi, SW-Iceland carbon storage site. International Journal of Greenhouse Gas Control 12, 399-418.

Amalokwu, K., Best, A.I., Sothcott, J., Chapman, M., Minshull, T., Li, X.-Y., 2014. Water saturation effects on elastic wave attenuation in porous rocks with aligned fractures. Geophysical Journal International 197, 943-947.

Amorim, C.L.G., Lopes, R.T., Barroso, R.C., Queiroz, J.C., Alves, D.B., Perez, C.A., Schelin, H.R., 2007. Effect of clay–water interactions on clay swelling by X-ray diffraction. Nuclear Instruments and Methods in Physics Research Section A: Accelerators, Spectrometers, Detectors and Associated Equipment 580, 768-770.

Aradóttir, E.S.P., Sonnenthal, E.L., Björnsson, G., Jónsson, H., 2012. Multidimensional reactive transport modeling of CO_2 mineral sequestration in basalts at the Hellisheidi geothermal field, Iceland. International Journal of Greenhouse Gas Control 9, 24-40.

Archer, D., 2005. Fate of fossil fuel CO_2 in geologic time. Journal of Geophysical Research 110. DOI:10.1029/2004jc002625

Avizo, 2016. Avizo 3D Software User's Guide. FEI. https://www.fei.com/software/avizo-user-guide/ (accessed 07.07.2017).

Bernard, D., Nielsen, Ø., Salvo, L., Cloetens, P., 2005. Permeability assessment by 3D interdendritic flow simulations on microtomography mappings of Al–Cu alloys. Materials Science and Engineering: A 392, 112-120.

Berryman, J.G., 1992. Effective stress for transport properties of inhomogeneous porous rock. Journal of Geophysical Research: Solid Earth 97, 17409-17424.

Falcon-Suarez, I., North, L., Amalokwu, K., Best, A., 2016. Integrated geophysical and hydromechanical assessment for CO_2 storage: shallow low permeable reservoir sandstones. Geophysical Prospecting 64, 828-847.

Fisher, A.T., 1998. Permeability Within Basaltic Oceanic Crust. Reviews of Geophysics 36, 143-182.

Franzson, H., Zierenberg, R., Schiffman, P., 2008. Chemical transport in geothermal systems in Iceland. Journal of Volcanology and Geothermal Research 173, 217-229.

Gaus, I., 2010. Role and impact of CO_2-rock interactions during CO_2 storage in sedimentary rocks. International Journal of Greenhouse Gas Control 4, 73-89.

Gislason, S.R., Wolff-Boenisch, D., Stefansson, A., Oelkers, E.H., Gunnlaugsson, E., Sigurdardottir, H., Sigfusson, B., Broecker, W.S., Matter, J.M., Stute, M., 2010. Mineral sequestration of carbon dioxide in basalt: A pre-injection overview of the CarbFix project. International Journal of Greenhouse Gas Control 4, 537-545.

Goldberg, D., Slagle, A.L., 2009. A global assessment of deep-sea basalt sites for carbon sequestration. Energy Procedia 1, 3675-3682. DOI: 10.1016/j.egypro.2009.02.165

Goldberg, D.S., Kent, D.V., Olsen, P.E., 2010. Potential on-shore and off-shore reservoirs for CO_2 sequestration in Central Atlantic magmatic province basalts. Proceedings of the National Academy of Sciences of the United States of America 107, 1327-1332.

Hjartarson, Á., Sæmundsson, K., 2014. Geological Map of Iceland. Bedrock. 1:600 000: Iceland GeoSurvey.

Ketcham, R.A., Carlson, W.D., 2001. Acquisition, optimization and interpretation of X-ray computed tomographic imagery: applications to the geosciences. Computers & Geosciences 27, 381-400. DOI: 10.1016/s0098-3004(00)00116-3

Khalilabad, M.R., Axelsson, G., Gislason, S. R., 2008. Aquifer characterization with tracer test technique; permanent CO_2 sequestration into basalt, SW Iceland. Mineralogical Magazine 72, 121-125. DOI: 10.1180/minmag.2008.072.1.121

Le Quéré, C., Andrew, R.M., Canadell, J.G., Sitch, S., Korsbakken, J.I., Peters, G.P., Manning, A.C., Boden, T.A., Tans, P.P., Houghton, R.A., Keeling, R.F., Alin, S., Andrews, O.D., Anthoni, P., Barbero, L., Bopp, L., Chevallier, F., Chini, L.P., Ciais, P., Currie, K., Delire, C., Doney, S.C., Friedlingstein, P., Gkritzalis, T., Harris, I., Hauck, J., Haverd, V., Hoppema, M., Goldewijk, K.K., Jain, A.K., Kato, E., Kortzinger, A., Landschutzer, P., Lefevre, N., Lenton, A., Lienert, S., Lombardozzi, D., Melton, J.R., Metzl, N., Millero, F., Monteiro, P.M.S., Munro, D.R., Nabel, J.E.M.S., Nakaoka, S., O'brien, K., Olsen, A., Omar, A.M., Ono, T., Pierrot, D., Poulter, B., Rodenbeck, C., Salisbury, J., Schuster, U., Schwinger, J., Seferian, R., Skjelvan, I., Stocker, B.D., Sutton, A.J., Takahashi, T., Tian, H.Q., Tilbrook, B., Van Der Laan-Luijkx, I.T., Van Der Werf, G.R., Viovy, N., Walker, A.P., Wiltshire, A.J., Zaehle, S. 2016. Global Carbon Budget 2016. Earth System Science Data 8, 605-649.

Leu, L., Berg, S., Enzmann, F., Armstrong, R.T., Kersten, M., 2014. Fast X-ray Micro-Tomography of Multiphase Flow in Berea Sandstone: A Sensitivity Study on Image Processing. Transport in Porous Media 105, 451-469.

Marieni, C., Henstock, T.J., Teagle, D.A.H., 2013. Geological storage of CO_2 within the oceanic crust by gravitational trapping. Geophysical Research Letters 40, 6219-6224.

Matter, J.M., Stute, M., Hall, J., Mesfin, K., Snæbjörnsdóttir, S.Ó., Gislason, S.R., Oelkers, E.H., Sigfusson, B., Gunnarsson, I., Aradottir, E.S., Alfredsson, H.A., Gunnlaugsson, E., Broecker, W.S., 2013. Monitoring permanent CO_2 storage by in situ mineral carbonation using a reactive tracer technique. Energy Procedia 63, 4180–4185.

Matter, J.M., Stute, M., Snæbjörnsdottir, S.Ó., Oelkers, E.H., Gislason, S.R., Aradottir, E.S., Sigfusson, B., Gunnarsson, I., Sigurdardottir, H., Gunnlaugsson, E., Axelsson, G., Alfredsson, H.A., Wolff-Boenisch, D., Mesfin, K., Taya, D.F.d.l.R., Hall, J., Dideriksen, K., Broecker, W.S., 2016. Rapid carbon mineralization for permanent disposal of anthropogenic carbon dioxide emissions. Science 352, 1312-1314.

McGrail, B.P., Schaef, H.T., Ho, A.M., Chien, Y.-J., Dooley, J.J., Davidson, C.L., 2006. Potential for carbon dioxide sequestration in flood basalts. Journal of Geophysical Research: Solid Earth 111, B12201.

Mohan, K.K., Vaidya, R.N., Reed, M.G., Fogler, H.S., 1993. Water sensitivity of sandstones containing swelling and non-swelling clays. Colloids and Surfaces A: Physicochemical and Engineering Aspects 73, 237-254.

North, L., Best, A.I., Sothcott, J., MacGregor, L., 2013. Laboratory determination of the full electrical resistivity tensor of heterogeneous carbonate rocks at elevated pressures. Geophysical Prospecting 61, 458-470.

Oelkers, E.H., Gislason, S.R., Matter, J.M., 2008. Mineral Carbonation of CO_2. Elements 4, 333-337 DOI: 10.2113/gselements.4.5.333

Saar, M.O., Manga, M., 1999. Permeability-porosity relationship in vesicular basalts. Geophysical Research Letters 26, 111-114.

Schiffman, P., Fridleifsson, G.O., 1991. The smectite–chlorite transition in drillhole NJ-15, Nesjavellir geothermal field, Iceland: XRD, BSE and electron microprobe investigations. Journal of Metamorphic Geology 9, 679-696.

Schopka, H.H., Gudmundsson, M.T., Tuffen, H., 2006. The formation of Helgafell, southwest Iceland, a monogenetic subglacial hyaloclastite ridge: Sedimentology, hydrology and volcano–ice interaction. Journal of Volcanology and Geothermal Research 152, 359-377.

Sigfusson, B., Gislason, S.R., Matter, J.M., Stute, M., Gunnlaugsson, E., Gunnarsson, I., Aradottir, E.S., Sigurdardottir, H., Mesfin, K., Alfredsson, H.A., Wolff-Boenisch, D., Arnarsson, M.T., Oelkers, E.H., 2015. Solving the carbon-dioxide buoyancy challenge: The design and field testing of a dissolved CO_2 injection system. International Journal of Greenhouse Gas Control 37, 213-219.

Sigurdsson, Ó., Stefánsson, V., 1994. Reservoir parameters–Measurements from rock core (in Icelandic). National Energy Authority. OS-94049/JHD-28 B.

Snaebjornsdottir, S.O., Gislason, S.R., 2016. CO_2 storage potential of basaltic rocks offshore Iceland. Energy Procedia 86, 371-380. DOI: 10.1016/j.egypro.2016.01.038

Snæbjörnsdóttir, S.Ó., Oelkers, E.H., Mesfin, K., Aradóttir, E.S., Dideriksen, K., Gunnarsson, I., Gunnlaugsson, E., Matter, J.M., Stute, M., Gislason, S.R., 2017. The chemistry and saturation states of subsurface fluids during the in situ mineralisation of CO_2 and H_2S at the CarbFix site in SW-Iceland. International Journal of Greenhouse Gas Control 58, 87-102.

Snæbjörnsdóttir, S.Ó., Wiese, F., Fridriksson, T., Ármansson, H., Einarsson, G.M., Gislason, S.R., 2014. CO_2 storage potential of basaltic rocks in Iceland and the oceanic ridges. Energy Procedia 63, 4585-4600.

Wolff-Boenisch, D., Wenau, S., Gislason, S.R., Oelkers, E.H., 2011. Dissolution of basalts and peridotite in seawater, in the presence of ligands, and CO_2: Implications for mineral sequestration of carbon dioxide. Geochimica Et Cosmochimica Acta 75, 5510-5525.

Youssef, S., Rosenberg, E., Gland, N., Skalinski, M., Vizika, O., 2007. High Resolution CT and Pore-Network Models to Assess Petrophysical Properties of Homogeneous and Heterogeneous Carbonates. Society of Petroleum Engineers, 1-12. DOI: 10.2118/111427-ms

Supplementary Figures

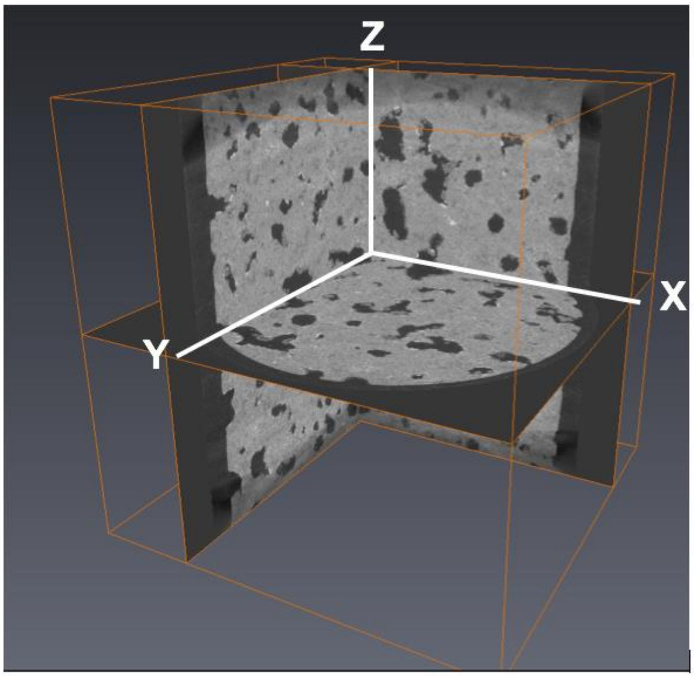

Figure 1. Basalt sub-sample 2 with visible edge streak noise artefacts. Edge streaks need to be removed from the data due to their anomalous grey-level intensity values compared to the rest of the sub-sample volume. Edge streaks occur due to a lower attenuation at the sample edge created by a shorter X-ray path length at the sample edge.

Supplementary Figures

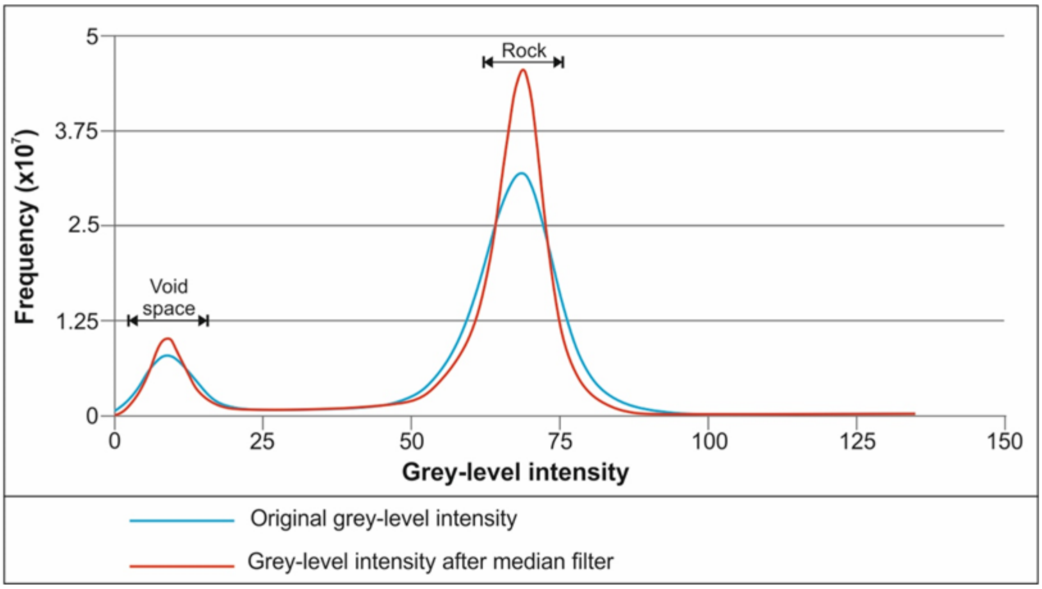

Figure 2. Frequency distribution graph of the 8 bit grey-level intensity, indicating the two main phases present within the basalt sample, void space and rock. The frequency distribution is of region of interest (ROI) sub-volume 2, however sub-volume 1 and 3 showed the same bimodal distribution. The two different lines represent the image prior to the application of a median filter (blue) and after filtering (red), showing how filtering improves phase distinction. The distribution has 256 grey-level intensity bin intervals, ranging from 0 to 135.

Supplementary Figures

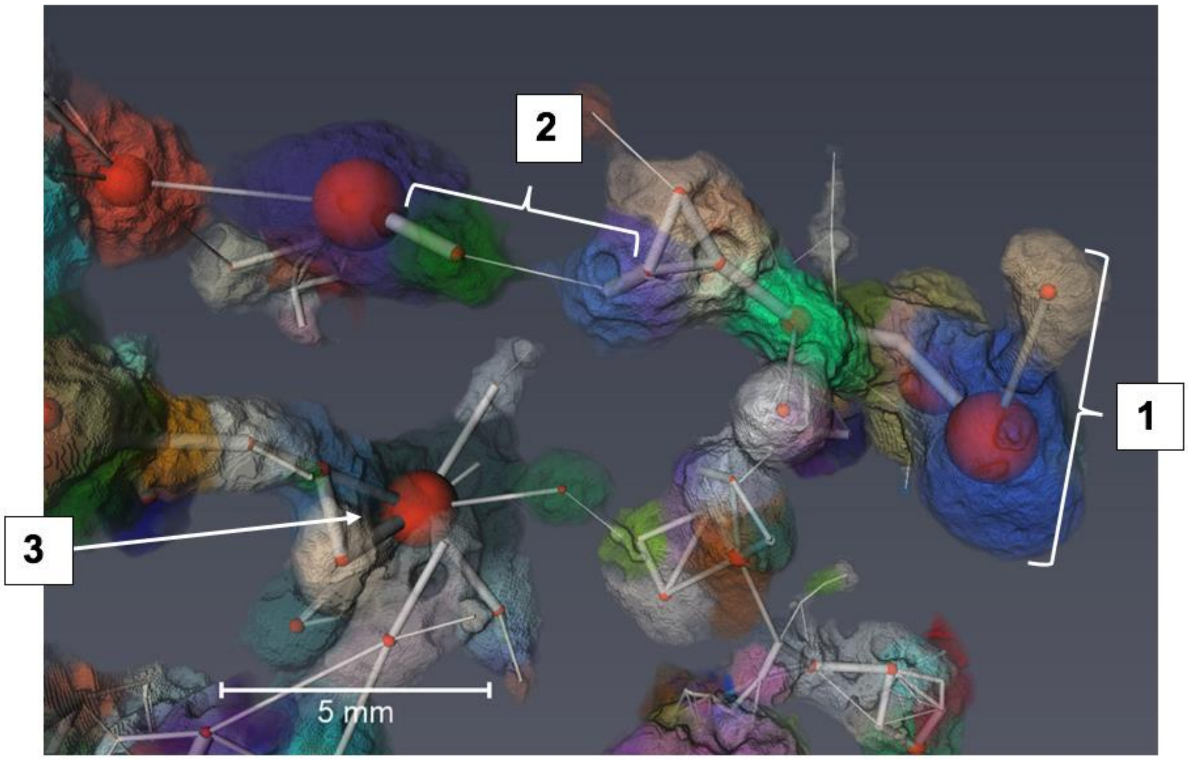

Figure 3. Volume rendering of the pore network model overlaid by the pore separation of the connected porosity of sub-sample 2, created using a skeletonization algorithm. The image highlights: (**1**) Relative pore volume, (**2**) relative throat / channel radii and (**3**) highly connected pores.

Supplementary Figures

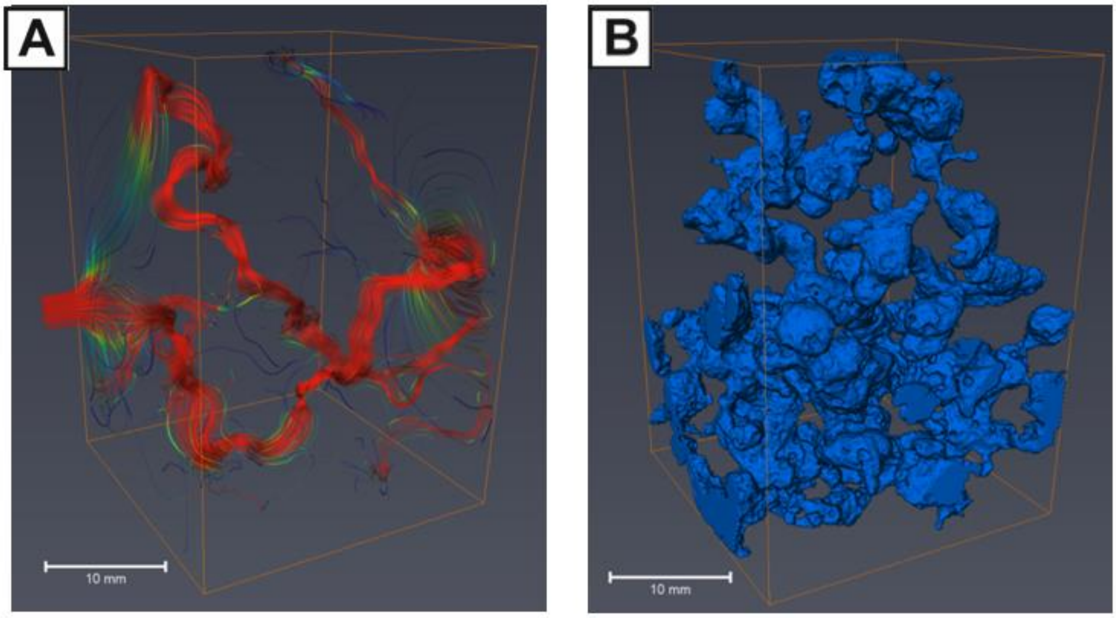

Figure 4. (**A**) Volume rendering illustration of the velocity field model from the horizontal absolute permeability simulation in 3D view. The colourmap displays areas of higher velocity fluid flow (red) and lower velocity fluid flow (blue). (**B**) Volume rendering of the connected pore space of basalt sub-sample 2.

Supplementary Figures

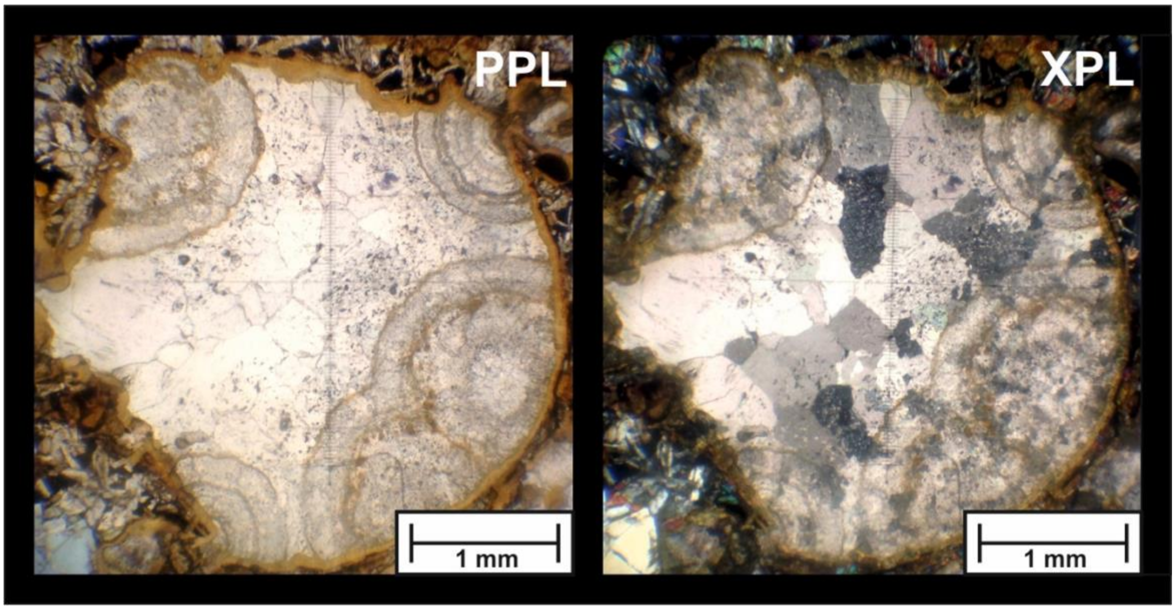

Figure 5. Thin section / Photomicrograph of secondary mineral carbonate precipitation in void space, observed in both plane polarised light (PPL) and cross polarised light (XPL).

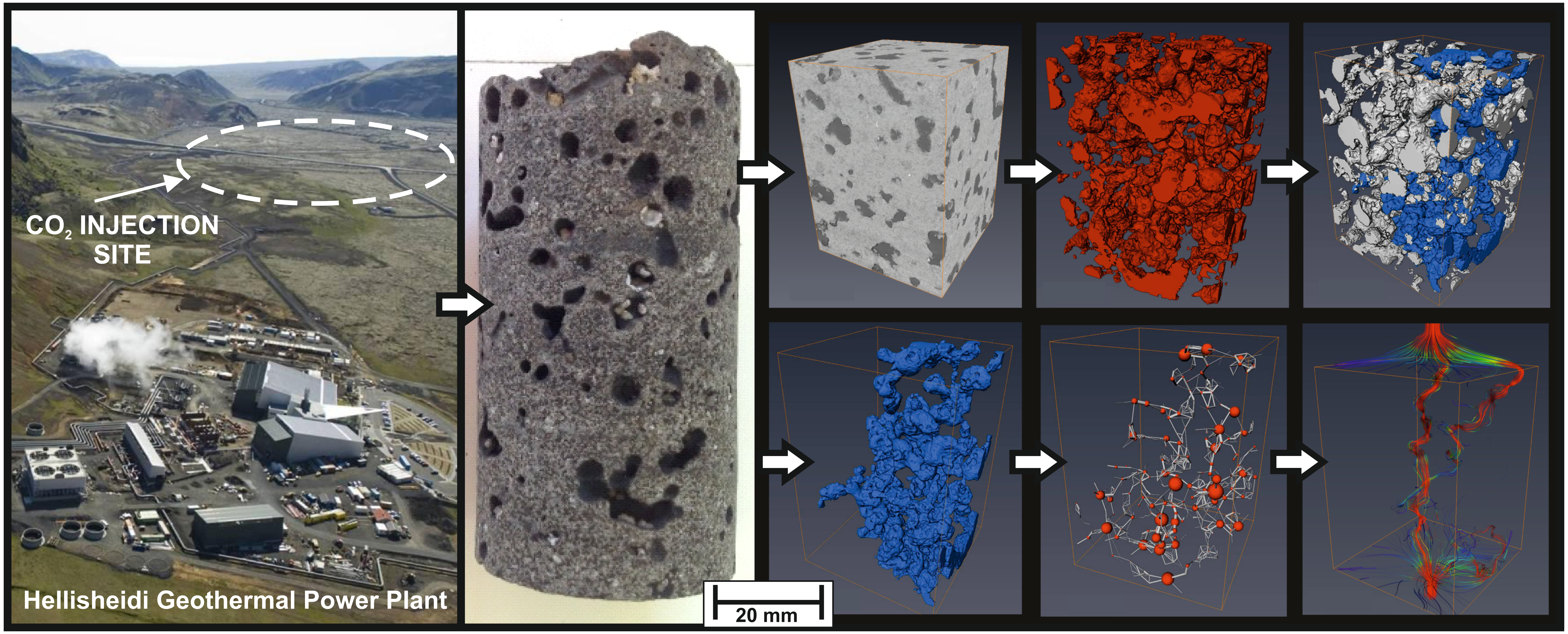
CO$_2$ INJECTION SITE
Hellisheidi Geothermal Power Plant
20 mm

HIGHLIGHTS

CO_2 mineral carbonation storage capacity and reservoir properties of basalt assessed

3D X-Ray micro-CT image analysis of core samples determine pore network properties

Hydromechanical tests show stress dependency of permeability at reservoir pressures

Calculated CO_2 storage capacity of 0.33 Gt CO_2 at CarbFix site in Iceland

Secondary mineral pore clogging may reduce CO_2 storage capacity of basalt reservoirs